

Highly Conductive and Porous Activated Reduced Graphene Oxide Films for High-Power Supercapacitors

Li Li Zhang,[†] Xin Zhao,^{†,‡} Meryl D. Stoller,[†] Yanwu Zhu,^{†,§} Hengxing Ji,[†] Shanthi Murali,[†] Yaping Wu,[†] Stephen Perales,[†] Brandon Clevenger,[†] and Rodney S. Ruoff^{†,*}

[†]Department of Mechanical Engineering and the Materials Science and Engineering Program, The University of Texas at Austin, One University Station C2200, Austin, Texas 78712, United States

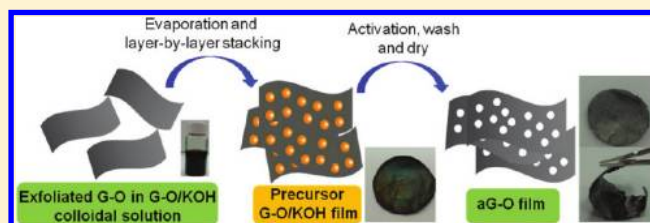
[‡]State Key Laboratory for Modification of Chemical Fibers and Polymer Materials, College of Materials Science and Engineering, Donghua University, Shanghai, 201620, P. R. China

[§]Department of Materials Science and Engineering, University of Science and Technology of China, Hefei, 230036, P. R. China

S Supporting Information

ABSTRACT: We present a novel method to prepare highly conductive, free-standing, and flexible porous carbon thin films by chemical activation of reduced graphene oxide paper. These flexible carbon thin films possess a very high specific surface area of $2400 \text{ m}^2 \text{ g}^{-1}$ with a high in-plane electrical conductivity of 5880 S m^{-1} . This is the highest specific surface area for a free-standing carbon film reported to date. A two-electrode supercapacitor using these carbon films as electrodes demonstrated an excellent high-frequency response, an extremely low equivalent series resistance on the order of 0.1 ohm , and a high-power delivery of about 500 kW kg^{-1} . While higher frequency and power values for graphene materials have been reported, these are the highest values achieved while simultaneously maintaining excellent specific capacitances and energy densities of 120 F g^{-1} and 26 W h kg^{-1} , respectively. In addition, these free-standing thin films provide a route to simplify the electrode-manufacturing process by eliminating conducting additives and binders. The synthetic process is also compatible with existing industrial level KOH activation processes and roll-to-roll thin-film fabrication technologies.

KEYWORDS: Graphene, flexible film, chemical activation, supercapacitors



Free-standing thin film materials are of great interest. Electronic and wearable devices, optical coatings, membrane filtration, energy storage, and conversion are only a few examples among the many applications that benefit from thin film technology. Carbon-based thin films have attracted considerable attention in view of their potential for use in flexible displays, as electrodes in electrical energy storage systems, and as transparent conducting films.^{1–5} Graphene, an atom-thick two-dimensional (2D) carbon nanostructure, with promising mechanical, thermal, chemical, and electrical properties, is of current interest.^{6–11} Previous efforts have demonstrated various filmlike structures, such as papers,^{6,12} thin films,^{13–15} and other 2D composite materials.^{10,16–18} However, the fabrication of free-standing flexible thin films based on or derived from graphene that are both highly electrically conductive and highly porous is an exciting challenge.

Free-standing graphene oxide (G-O) “papers” can be obtained by flow-directed assembly of well-exfoliated graphene oxide sheets, and the mechanical properties of such papers were studied.⁶ Recently, a highly porous graphene-derived carbon material based on KOH activation of microwave-exfoliated graphite oxide (MEGO) was discovered that we called “a-MEGO”.¹⁹ Extremely high Brunauer–Emmett–Teller (BET)

surface areas of up to $3100 \text{ m}^2 \text{ g}^{-1}$ and powder electrical conductivity values of up to 500 S m^{-1} were obtained for a-MEGO, and it showed superb energy density values but with the typical time response of a supercapacitor (i.e., seconds).¹⁹ Miller et al. developed a supercapacitor (the term is synonymous with ultracapacitor) having oriented and relatively sparsely distributed graphene flakes grown on nickel by CVD.²⁰ Their graphene nanosheets showed efficient filtering of 120 Hz current with an RC time constant of less than 0.2 ms , but at the cost of very low energy density and capacitance.

Inspired by the above, we have prepared activated reduced graphene oxide films that we name “aG-O”, and we describe this new film material here. The aG-O material is a flexible free-standing porous carbon film with high specific surface areas of up to $2400 \text{ m}^2 \text{ g}^{-1}$ and a very high in-plane electrical conductivity of 5880 S m^{-1} . Combustion elemental analysis revealed a very low H content of less than $0.5 \text{ wt } \%$ and a high C/O atomic ratio of 14, higher than that found for typical “chemically converted” graphene sheets.¹² The XPS spectra (Figure S1) also showed low oxygen content. Scheme 1

Received: November 6, 2011

Revised: January 31, 2012

Published: February 28, 2012

Scheme 1. Schematic Illustration Showing the Experimental Steps of aG-O Film

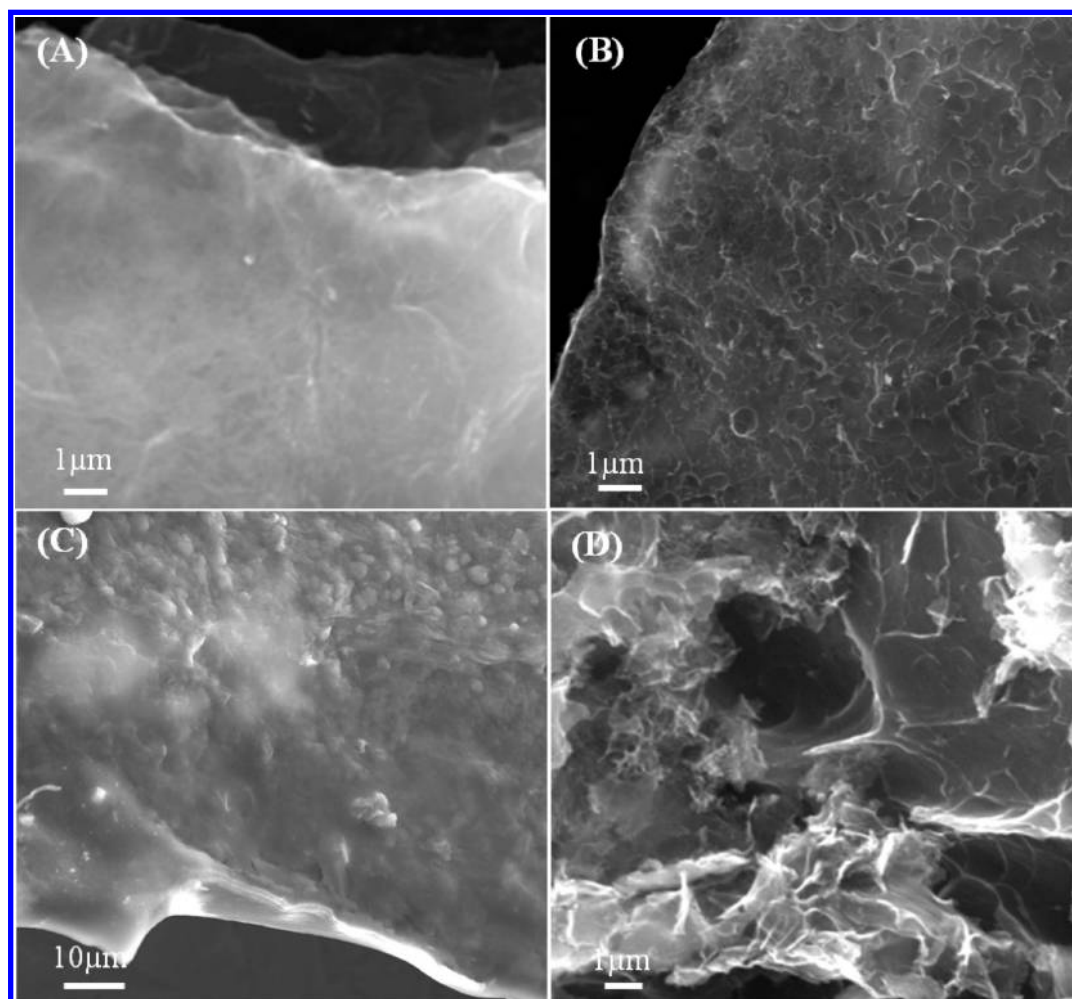
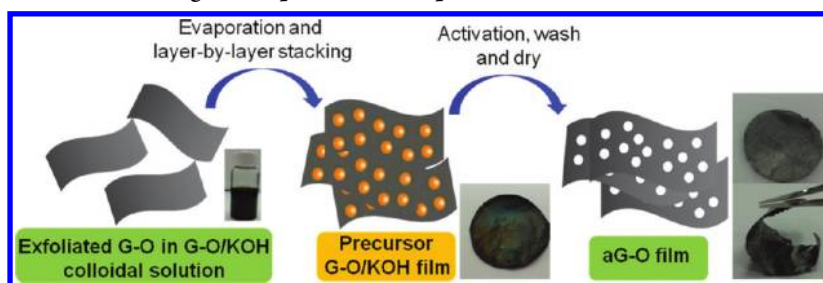


Figure 1. SEM images showing the surface morphology of (A) aG-O14 film, (B) aG-O16 film, (C) the precursor G-O/KOH film, and (D) an a-MEGO “chunk”.

illustrates the process steps for the preparation of the filmlike materials. First, an aqueous colloidal suspension was prepared by addition of 1 M KOH dropwise into 1 mg mL⁻¹ of G-O colloidal suspension; such a colloid contains graphene oxide platelets suspended in the water with KOH dissolved in the water. This water was then evaporated by heating in an oil bath at 100 °C under constant stirring until it thickened into an “ink paste”. The paste consists of G-O platelets dispersed with KOH in some remaining water. Films composed of stacked and overlapped G-O platelets decorated with KOH (Figure S2 shows the scanning electron microscopy (SEM) images of these precursor G-O/KOH films with both top-down and cross-sectional views) were obtained through brief vacuum filtration (using a SterliTech PTFE membrane filter) under

directional flow followed by drying. Next, an activation step similar to that described in our previous report¹⁹ was carried out in which the dry film was placed in a quartz tube furnace under flowing argon at 800 °C for 1 h and a pressure of 1 atm. The final free-standing aG-O films with thicknesses ranging from 7 to 30 μm were obtained after washing and drying (see Supporting Information for details). The concentration of KOH is crucial in achieving a homogeneous colloidal solution (the homogeneity of the solution is essential for the layer-to-layer assembly to get oriented films) as excess KOH results in an immediate precipitation of G-O platelets in the solution. The free-standing aG-O films are flexible and have a metallic luster (Scheme 1). The film electrodes have a relatively smooth surface, are uniform in thickness, and can be bent and cut to

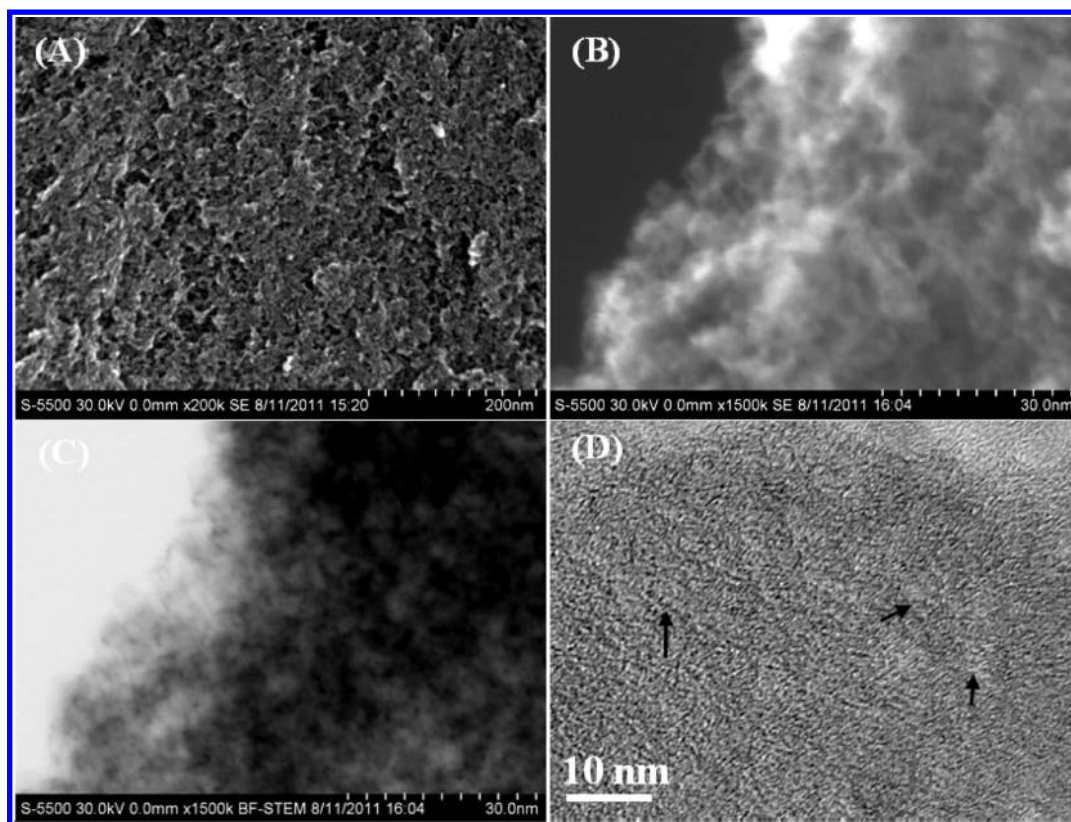


Figure 2. (A) High-resolution SEM image of aG-O14 film that demonstrates its porous structure. (B) SEM image of aG-O14 film and (C) the corresponding ADF-STEM image of the same region as in (B). (D) High-resolution TEM image of aG-O14 film. The presence of the uniform micropores smaller than 2 nm are clearly observed (some are indicated by the black arrows).

different shapes and sizes. In contrast, dark “cakes” or “delaminated papers” would be obtained from nonhomogeneous suspensions, and thus we emphasize the importance of a careful control over the KOH concentration (Figure S3).

The role of KOH in the chemical activation of carbons has been extensively studied,¹⁹ and the use of KOH is a common and practical way to produce activated carbons at an industrial scale. A series of KOH activated reduced graphene oxide films were prepared in this work. The degree of activation was controlled by the mass ratio of KOH to G-O platelets (Figure S4). The surface morphologies of the aG-O films and the precursor G-O/KOH film was observed using SEM and are shown in Figure 1. A flat and continuous sheetlike structure was seen for aG-O samples (Figure 1A,B), in great contrast to the a-MEGO chunk (Figure 1D). Due to the different mass loading of KOH for activation, the aG-O14 film (the sample that was obtained with a mass ratio of KOH/G-O platelets of 14) had a continuous film structure with dense micropores (see Figure 2) while the aG-O16 film (KOH/G-O ratio is 16) had a rough surface with severe etching by the larger quantity of KOH. (More images showing the more extensive digestion of the aG-O16 film by the excessive amount of KOH are shown in Figure S5.) The morphology of the precursor film was found to directly influence the final structure of the aG-O films. “Continuous” precursor films with KOH well intercalated between the G-O platelets are shown in Figure 1C and Figure S2. As mentioned above, a stable colloidal suspension is essential for the subsequent assembly to produce a continuous precursor film with KOH well dispersed between G-O platelets prior to the activation process.

We note that a partial reduction of G-O by KOH during the formation of the precursor film was observed. Thermal gravimetric analysis (TGA) of the G-O/KOH precursor film in air (Figure S6) showed less than a 5 wt % loss between 100 and 300 °C, which is the typical temperature range for the removal of oxygen-containing functional groups from graphene oxide. This suggested that most of the functional groups were removed by the interaction with KOH during the evaporation process. Other studies have also reported the reduction of G-O by KOH.^{21,22} A control experiment was performed to produce a KOH-reduced G-O film sample by repeatedly washing the precursor G-O/KOH film with DI water and 10 wt % acetic acid. The C1s XPS spectra of the KOH-reduced film and of as-prepared G-O film are shown in Figure S7; the peak intensity of C=O is dramatically decreased by the KOH reduction as compared to that of the as-prepared G-O film, indicating efficient deoxygenation of G-O platelets by KOH during the evaporation process. The small XPS peak at about 288.5 eV indicates there was a small amount of carboxyl group functionality left in the sample. It also shows that KOH merely removed the functional groups during this step. (The precursor G-O/KOH film had no obvious pores present as shown in Figure 1C and Figure S2.) The etching or activation of carbon, as expected, occurs through the high temperature process.

The highly porous and interconnected three-dimensional (3D) microstructure of the aG-O14 film was readily observed from the high-resolution SEM images (Figure 2A,B) and the corresponding annular dark field scanning transmission electron microscopy (ADF-STEM) image (Figure 2C). As seen, the aG-O14 film contained a substantial amount of micro- and mesopores that are homogeneously distributed throughout

the highly porous structure. The high-resolution transmission electron microscopy (HR-TEM) image (Figure 2D) further demonstrated the presence of the dense micropores along with small mesopores that are less than 5 nm (some are indicated by the black arrows).

The nitrogen adsorption–desorption isotherms of various aG-O samples are shown in Figure 3A. The strong nitrogen

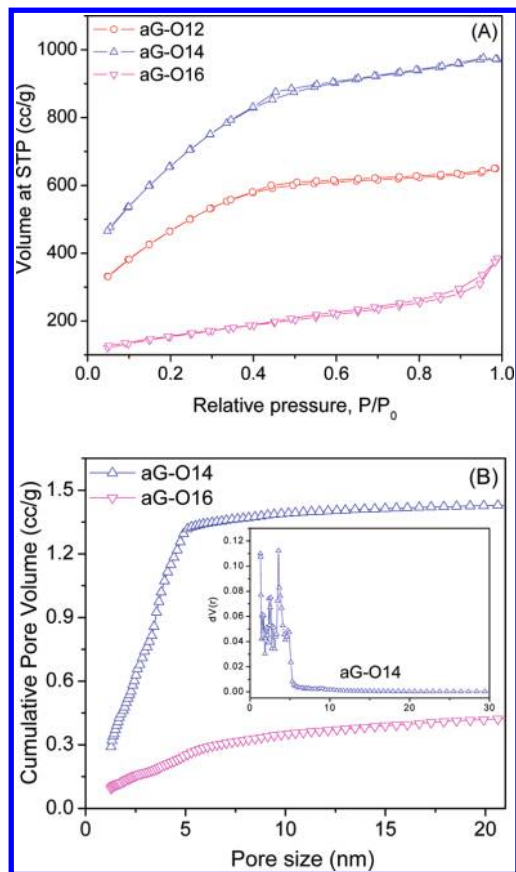


Figure 3. Nitrogen adsorption/desorption analysis of aG-O films. (A) Isotherms of various aG-O films and (B) cumulative pore volume and pore size distribution (inset) calculated using a slit/cylindrical NLDFT model.

adsorption below the relative pressure of $P/P_0 = 0.1$ for aG-O12 and aG-O14 is a feature of micropore filling.²³ The continuous rise of the isotherms in the relative pressure range from 0.1 to 0.6 combined with the decreased slope above 0.6 implied the presence of an appreciable amount of mesopores for both aG-O12 and aG-O14 samples. In contrast, an abrupt nitrogen uptake at $P/P_0 > 0.9$ for aG-O16 revealed the textural porosity due to the rough sheet surface caused by the excessive KOH activation, in accordance with the SEM observation (Figure 1B). The cumulative pore volume (Figure 3B) for the aG-O14 film reached over 90% of the total pore volume from pores smaller than 5 nm. Pores smaller than 5 nm accounted for only 60% of the total volume for sample aG-O16, indicating considerable contribution from large mesopores and/or the textural macropores. The pore size distribution of aG-O14 sample derived from the slit/cylindrical nonlocal density functional theory (NLDFT) showed a sharp peak around 1 nm for micropores with another narrow peak centered at ~ 3.6 nm for mesopores. The BET surface area is as high as $2400 \text{ m}^2 \text{ g}^{-1}$ with a total pore volume of $1.5 \text{ cm}^3 \text{ g}^{-1}$ for aG-O12 film,

and to our knowledge this is the highest for a free-standing carbon film material reported to date.

The electrical conductivity of the aG-O films was measured using a two-probe method, and the results are shown in Figure 4. A strong dependence between the conductivity, film

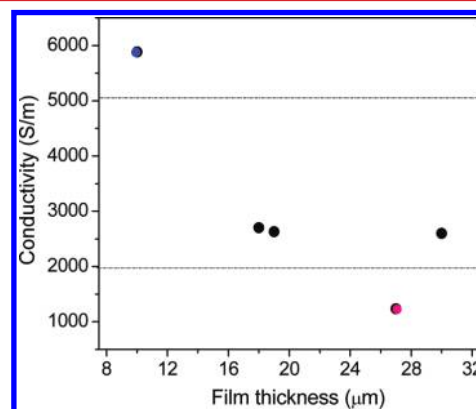


Figure 4. Electrical conductivities for various aG-O films at different film thickness and porosity.

thickness, and the porosity was found for the aG-O films. For the very thin film with a thickness less than $10 \mu\text{m}$, the conductivity was as high as 5880 S m^{-1} even with a relatively high BET surface area of $1700 \text{ m}^2 \text{ g}^{-1}$ (indicated by a blue point), indicating a highly continuous and well-interconnected 3D porous network. For the films with thicknesses between 10 and $30 \mu\text{m}$ (BET surface areas ranging from 1360 to $2400 \text{ m}^2 \text{ g}^{-1}$), typical conductivities ranged between 2000 and 3000 S m^{-1} , with one exception (denoted as a pink point with the conductivity of 1230 S m^{-1}). This relatively lower conductivity point (aG-O16 film) is attributed to the excessive KOH activation, causing some degree of discontinuity of the porous film structure. Nevertheless, the conductivity of the aG-O films is still much higher than powder materials and is comparable to chemically modified single-walled carbon nanotube paper²⁴ and chemically converted graphene sheets but with a much more developed porosity.¹² The well-defined micro- and mesopores evenly distributed in a three-dimensionally continuous sheetlike porous structure are expected to have fast ion and charge transfer, desirable in many applications, particularly as supercapacitor electrodes.

The electrochemical performance of the aG-O film based electrodes was analyzed using best practice methods;²⁵ a two-electrode symmetrical supercapacitor cell was constructed using both aqueous (KOH) and organic (tetraethylammonium tetrafluoroborate (TEABF₄) in acetonitrile (AN)) electrolytes.²⁶ The CV curves were measured with various scan rates ranging from 5 to 400 mV s^{-1} . The near-rectangular CV curves (Figure 5A) and triangular shape of the charge/discharge plots (Figure 5B) in 1 M KOH electrolyte indicated small mass-transfer resistance and good charge propagation behavior of ions in the porous aG-O film electrode. The rate-dependent surface area normalized capacitance is shown in Figure 5C. The BET surface area normalized capacitance at all the studied scan rates is greater than $11 \mu\text{F cm}^{-2}$. More importantly, the area normalized capacitance only decreased slightly from 14 to $11 \mu\text{F cm}^{-2}$ when the scan rate was increased 8-fold from 50 to 400 mV s^{-1} , indicating an efficient EDL formation within the porous thin film structure at high rate.²⁷ This high rate performance of the aG-O thin film electrode is closely related

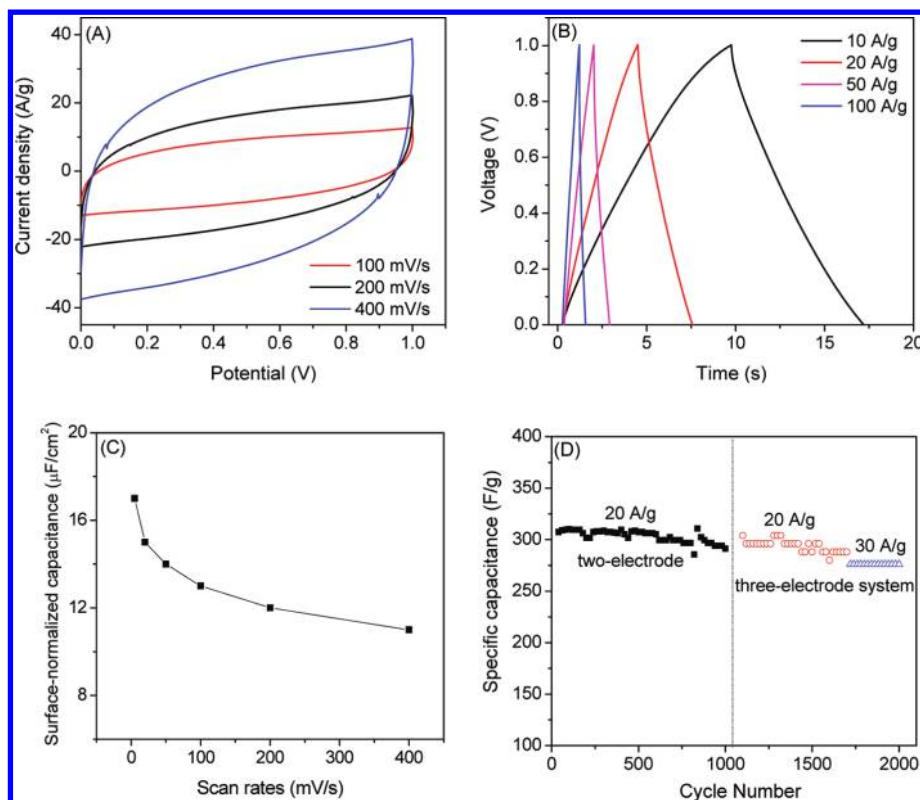


Figure 5. Electrochemical performance of the aG-O14 film electrode in 1 M KOH solution. (A) CV curves at various scan rates. (B) Galvanostatic charge/discharge curves under different current densities. (C) Gravimetric capacitance and surface-area normalized capacitance at various scan rates. (D) Cycle stability tests in both two-electrode and three-electrode configurations under various current loadings.

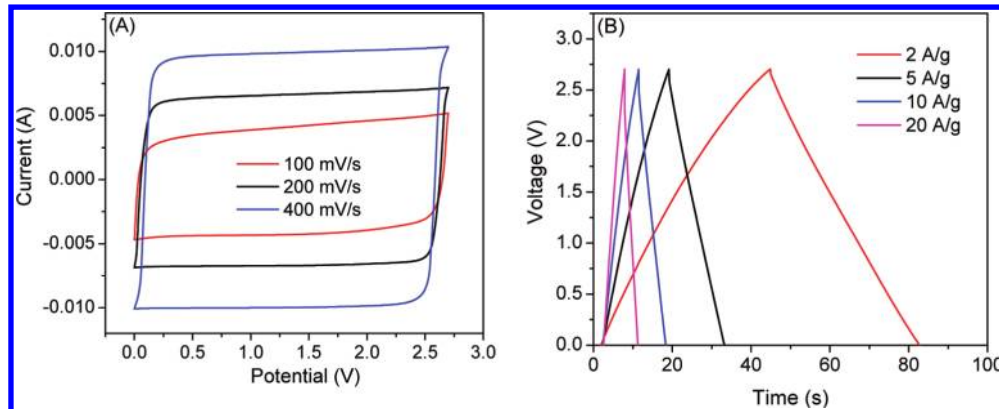


Figure 6. Electrochemical performance of aG-O14 film electrode in TEA BF₄/AN solution. (A) CV curves at various scan rates. (B) Galvanostatic charge/discharge curves under different current densities.

to its unique binder-free porous thin film structure.²⁸ The highly interconnected 3D structure and short diffusion pathway favor fast charge transportation. The cycling performance of the aG-O14 film (Figure 5D) showed negligible capacitance degradation ($\sim 95\%$ capacitance retention) after 2000 cycles (Figure S8), indicating a very stable electrode material.

A similar two-electrode cell was constructed using aG-O14 film as the electrode material and TEABF₄/AN as the electrolyte and the performance is shown in Figure 6. The almost perfect rectangular CV curves at ultrafast sweep rate of 400 mV s^{-1} indicated very efficient charge transfer within the porous film electrodes. The symmetrical triangles of the charge/discharge plots with small IR drops indicated an ideal EDLC behavior of the porous thin film electrode. The Ragone

plots displayed in Figure 7 clearly demonstrate the ultrahigh-power performance of the aG-O films in both organic and aqueous electrolytes. A very high power density of about 500 kW kg^{-1} was achieved with a reasonably high energy density of 26 W h kg^{-1} (specific capacitance of 120 F g^{-1} at the current density of 10 A g^{-1} for aG-O14 film) with free-standing aG-O film as the electrode in the TEABF₄/AN system.

To further understand the superior power performance of these aG-O film electrodes, the kinetic feature of the ion diffusion in the porous film electrode was investigated using electrochemical impedance spectroscopy in both aqueous electrolyte and organic electrolyte systems. Figure 8A shows the Nyquist plot obtained in 1 M KOH at the frequency range from 1000 kHz to 0.01 Hz, with an expanded view of the high-

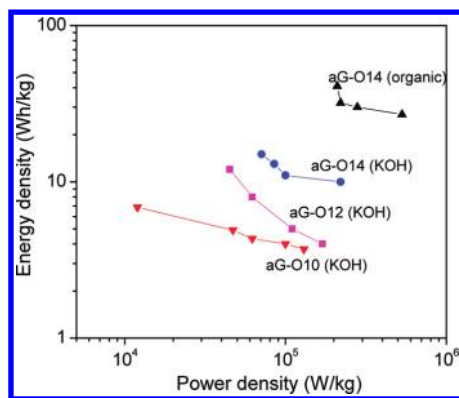


Figure 7. Ragone plots showing the energy density and power density for various aG-O film electrodes in both aqueous and organic electrolytes.

frequency region in the inset. The near-vertical slope at the low-frequency region indicates a good capacitor behavior of the cell. The negligible high-frequency resistor–capacitor (RC) loop or semicircle shows good electrode contact.^{20,29} The equivalent series resistance obtained from the x -intercept of the Nyquist plot (Figure 8A inset) is extremely small at ~ 0.1 ohm, very close to and even slightly smaller than that reported for a thin carbon nanotube sheet electrode,³⁰ suggesting that the aG-O film electrodes have very small resistance with good ion response. The impedance curve intersects the real axis at a 45° angle, which is the typical feature of a porous electrode when saturated with electrolyte.³⁰

An impedance phase angle plot is shown in Figure 8B. The near -90° phase angle at low frequencies indicates capacitive behavior and 90° phase angles at high frequency indicates inductive behavior. Most supercapacitors show a similar capacitor-to-inductor transition under ac frequencies as the frequency increases.^{20,31} A unique feature of these aG-O film-based supercapacitors is that the transition occurred in a narrow and high frequency range between 10^4 and 10^5 Hz, in great contrast to the transition observed with activated carbon-based supercapacitors that typically covers several decades from the low- to high-frequency region (typically from 1 to 10^5).^{20,30,31}

The excellent electron conductive properties of the aG-O film electrode in organic electrolyte can be readily seen from Figure 9. Two aluminum sheets were used both as the current collector and also as the metal electrode, in a two-electrode configuration using TEABF₄/AN as the electrolyte. In

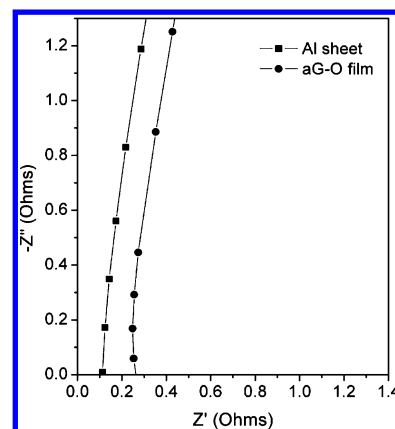


Figure 9. Complex-plane impedance in organic electrolyte. A single-cell capacitor fabricated with aG-O film used both as the electrode and also as the current collector, compared to a similar configuration but with aluminum sheet used both as the electrode and also as the current collector.

comparison, a cell was assembled using two free-standing aG-O films both as the current collector and also as the electrode, respectively, in a similar system. The series equivalent resistance of the single-cell test device fabricated with aG-O film was about 0.3 ohm, only slightly higher than that of the cell having aluminum sheets. This further demonstrates the excellent electronic conducting properties of the aG-O film.

In summary, we have developed a method to prepare highly conductive, free-standing, and flexible porous carbon films by simple KOH activation of reduced G-O films. Our method is compatible with existing industrial KOH activation processes and roll-to-roll thin-film fabrication technology. The free-standing thin films can simplify the electrode-manufacturing process by eliminating the addition of conducting additives and binders. These films have the highest measured specific surface area reported to date for a free-standing carbon film, and supercapacitors constructed with these films as electrodes yielded outstanding power and frequency performance while simultaneously maintaining excellent energy densities. Moreover, the new carbon material's physical and chemical properties (such as high conductivity, highly developed surface area, open pore structure, chemical stability, and flexibility) make them not only suitable for high-power energy storage but also candidates for other applications such as lithium ion

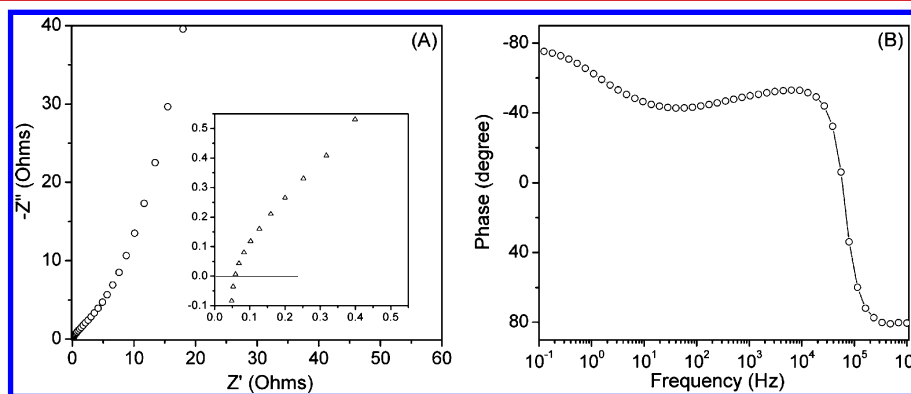


Figure 8. (A) Nyquist plot showing the imaginary part versus the real part of impedance. Inset shows the high-frequency region of the plot. (B) Impedance phase angle versus frequency for aG-O14 film.

batteries, conducting substrates for composites, photocatalysis, and so on.

■ ASSOCIATED CONTENT

■ Supporting Information

Experimental details, SEM images, TEM images, TGA analysis data, and XPS of samples. This material is available free of charge via the Internet at <http://pubs.acs.org>.

■ AUTHOR INFORMATION

Corresponding Author

*E-mail: r.ruoff@mail.utexas.edu.

Notes

The authors declare no competing financial interest.

■ ACKNOWLEDGMENTS

We appreciate funding support from the U.S. Department of Energy (DOE) under award DE-SC0001951 and the Institute of Advanced Technology.

■ REFERENCES

- (1) Li, X.; Zhu, Y.; Cai, W.; Borysiak, M.; Han, B.; Chen, D.; Piner, R. D.; Colombo, L.; Ruoff, R. S. *Nano Lett.* **2009**, *9* (12), 4359–4363.
- (2) Avouris, P.; Chen, Z.; Perebeinos, V. *Nat. Nanotechnol.* **2007**, *2* (10), 605–615.
- (3) Chen, Z.; Ren, W.; Gao, L.; Liu, B.; Pei, S.; Cheng, H.-M. *Nat. Mater.* **2011**, *10* (6), 424–428.
- (4) Wu, Q.; Xu, Y.; Yao, Z.; Liu, A.; Shi, G. *ACS Nano* **2010**, *4* (4), 1963–1970.
- (5) Yu, A.; Roes, I.; Davies, A.; Chen, Z. *Appl. Phys. Lett.* **2010**, *96*, 25.
- (6) Dikin, D. A.; Stankovich, S.; Zimney, E. J.; Piner, R. D.; Dommett, G. H. B.; Evmenenko, G.; Nguyen, S. T.; Ruoff, R. S. *Nature* **2007**, *448* (7152), 457–460.
- (7) Geim, A. K.; Novoselov, K. S. *Nat. Mater.* **2007**, *6* (3), 183–191.
- (8) Zhu, Y. W.; Murali, S.; Cai, W. W.; Li, X. S.; Suk, J. W.; Potts, J. R.; Ruoff, R. S. *Adv. Mater.* **2010**, *22* (46), 5226–5226.
- (9) Zhang, L. L.; Zhou, R.; Zhao, X. S. *J. Mater. Chem.* **2010**, *20* (29), 5983–5992.
- (10) Stankovich, S.; Dikin, D. A.; Dommett, G. H. B.; Kohlhaas, K. M.; Zimney, E. J.; Stach, E. A.; Piner, R. D.; Nguyen, S. T.; Ruoff, R. S. *Nature* **2006**, *442* (7100), 282–286.
- (11) Park, S.; Ruoff, R. S. *Nat. Nanotechnol.* **2009**, *4* (4), 217–224.
- (12) Li, D.; Muller, M. B.; Gilje, S.; Kaner, R. B.; Wallace, G. G. *Nat. Nanotechnol.* **2008**, *3* (2), 101–105.
- (13) An, S. J.; Zhu, Y.; Lee, S. H.; Stoller, M. D.; Emilsson, T.; Park, S.; Velamakanni, A.; An, J.; Ruoff, R. S. *J. Phys. Chem. Lett.* **2010**, *1* (8), 1259–1263.
- (14) Eda, G.; Fanchini, G.; Chhowalla, M. *Nat. Nanotechnol.* **2008**, *3* (5), 270–274.
- (15) Li, X.; Zhang, G.; Bai, X.; Sun, X.; Wang, X.; Wang, E.; Dai, H. *Nat. Nanotechnol.* **2008**, *3* (9), 538–542.
- (16) Zhang, L. L.; Zhao, S.; Tian, X. N.; Zhao, X. S. *Langmuir* **2010**, *26* (22), 17624–17628.
- (17) Park, S.; Mohanty, N.; Suk, J. W.; Nagaraja, A.; An, J.; Piner, R. D.; Cai, W.; Dreyer, D. R.; Berry, V.; Ruoff, R. S. *Adv. Mater.* **2010**, *22* (15), 1736–1940.
- (18) Lee, S. H.; Kim, H. W.; Hwang, J. O.; Lee, W. J.; Kwon, J.; Bielawski, C. W.; Ruoff, R. S.; Kim, S. O. *Angew. Chem., Int. Ed.* **2010**, *49* (52), 10084–10088.
- (19) Zhu, Y.; Murali, S.; Stoller, M. D.; Ganesh, K. J.; Cai, W.; Ferreira, P. J.; Pirkle, A.; Wallace, R. M.; Cychoz, K. A.; Thommes, M.; Su, D.; Stach, E. A.; Ruoff, R. S. *Science* **2011**, *332* (6037), 1537–1541.
- (20) Miller, J. R.; Outlaw, R. A.; Holloway, B. C. *Science* **2010**, *329* (5999), 1637–1639.
- (21) Park, S.; An, J.; Piner, R. D.; Jung, I.; Yang, D.; Velamakanni, A.; Nguyen, S. T.; Ruoff, R. S. *Chem. Mater.* **2008**, *20* (21), 6592–6594.
- (22) Fan, X.; Peng, W.; Li, Y.; Li, X.; Wang, S.; Zhang, G.; Zhang, F. *Adv. Mater.* **2008**, *20* (23), 4490–4493.
- (23) Kruk, M.; Jaroniec, M. *Chem. Mater.* **2001**, *13* (10), 3169–3183.
- (24) Skákalová, V.; Kaiser, A. B.; Dettlaff-Weglikowska, U.; Hrnčariková, K.; Roth, S. *J. Phys. Chem. B* **2005**, *109* (15), 7174–7181.
- (25) Stoller, M. D.; Ruoff, R. S. *Energy Environ. Sci.* **2010**, *3* (9), 1294–1301.
- (26) Stoller, M. D.; Park, S.; Zhu, Y.; An, J.; Ruoff, R. S. *Nano Lett.* **2008**.
- (27) Largeot, C.; Portet, C.; Chmiola, J.; Taberna, P. L.; Gogotsi, Y.; Simon, P. *J. Am. Chem. Soc.* **2008**, *130* (9), 2730–2731.
- (28) Chmiola, J.; Largeot, C.; Taberna, P.-L.; Simon, P.; Gogotsi, Y. *Science* **2010**, *328* (5977), 480–483.
- (29) Portet, C.; Lillo-Rodenas, M. A.; Linares-Solano, A.; Gogotsi, Y. *Phys. Chem. Chem. Phys.* **2009**, *11* (25), 4943–4945.
- (30) Niu, C. M.; Sichel, E. K.; Hoch, R.; Moy, D.; Tennent, H. *Appl. Phys. Lett.* **1997**, *70* (11), 1480–1482.
- (31) Miller, J. R. Pulse power performance of electrochemical capacitors: technical status of present commercial devices. In 8th International Seminar on Double Layer Capacitors and Similar Energy Storage Devices, Florida, 1998.